

Suppression of Octahedral Tilts and Associated Changes in Electronic Properties at Epitaxial Oxide Heterostructure Interfaces

A. Y. Borisevich,^{1,*} H. J. Chang,¹ M. Huijben,^{2,3} M. P. Oxley,¹ S. Okamoto,¹ M. K. Niranjan,⁴ J. D. Burton,⁴ E. Y. Tsymbal,⁴ Y. H. Chu,⁵ P. Yu,³ R. Ramesh,³ S. V. Kalinin,¹ and S. J. Pennycook¹

¹Oak Ridge National Laboratory, Oak Ridge, Tennessee 37831, USA

²Faculty of Science and Technology, MESA⁺ Institute for Nanotechnology, University of Twente, P.O. Box 217, 7500 AE, Enschede, The Netherlands

³Department of Materials Science and Engineering and Department of Physics, University of California, Berkeley, California 94720, USA

⁴Department of Physics and Astronomy, Nebraska Center for Materials and Nanoscience, University of Nebraska, Lincoln, Nebraska 68588, USA

⁵Department of Materials Science and Engineering, National Chiao Tung University, Hsinchu, Taiwan 30013, Republic of China
(Received 10 February 2010; published 19 August 2010)

Epitaxial oxide interfaces with broken translational symmetry have emerged as a central paradigm behind the novel behaviors of oxide superlattices. Here, we use scanning transmission electron microscopy to demonstrate a direct, quantitative unit-cell-by-unit-cell mapping of lattice parameters and oxygen octahedral rotations across the BiFeO₃-La_{0.7}Sr_{0.3}MnO₃ interface to elucidate how the change of crystal symmetry is accommodated. Combined with low-loss electron energy loss spectroscopy imaging, we demonstrate a mesoscopic antiferrodistortive phase transition near the interface in BiFeO₃ and elucidate associated changes in electronic properties in a thin layer directly adjacent to the interface.

DOI: 10.1103/PhysRevLett.105.087204

PACS numbers: 75.85.+t, 68.37.Ma, 68.65.-k, 79.20.Uv

The unique electronic and dielectric properties of oxide heterostructures have recently propelled these systems to the forefront of condensed matter physics. Controlling charge transfer across the interfaces gives rise to spectacular behaviors including interface mediated conduction [1], superconductivity [2], magnetic effects [3], and improper ferroelectric responses [4]. However, the full spectrum of electronic behaviors at ferroelectric-oxide interfaces, including interface reconstructions and coupling to octahedral rotations, remains enigmatic and largely unexplored.

Here we utilize direct structural mapping [5,6] by high-resolution scanning transmission electron microscopy (STEM) to determine lattice parameters and oxygen octahedral rotations at an epitaxial BiFeO₃-La_{0.7}Sr_{0.3}MnO₃ (BFO-LSMO) interface combined with electronic structure imaging by electron energy loss spectroscopy (EELS) [7]. This allows us to directly correlate the atomic structure, polarization, strain fields, and dielectric behavior on the atomic level. Combined with density functional calculations the data reveal the formation of a mesoscopic interface-induced phase at the BFO-LSMO interface such that a thin layer of BFO transforms into a phase with reduced band gap or possibly metallic behavior.

Multiferroic BiFeO₃ (BFO) was grown on a ferromagnetic La_{0.7}Sr_{0.3}MnO₃ electrode in the (100) orientation [8]. While bulk rhombohedral BiFeO₃ is ferroelectric and antiferromagnetic, the presence of strong electric fields in major crystallographic directions [9] or pressure [10] could stabilize high-symmetry metallic [11] (or low band-gap) phases. Notably, in BFO the octahedral tilts are related to the Fe-O-Fe angles and high or low spin states of Fe atoms,

and hence directly control the metal-insulator transitions and magnetic properties [12].

Here, we build an integrated picture of local structural distortions in the vicinity of the interface by directly measuring lattice parameter changes and octahedral rotation angles for every unit cell. To that end we use atomic position quantification from aberration corrected STEM images, building upon the approach recently introduced by Jia *et al.* [5,6,13] for TEM images. Shown in Fig. 1(a) is the high angle annular dark field (HAADF) STEM image of the SrTiO₃ (STO)/5 nm LSMO/50 nm BFO heterostructure (STO is outside of the field of view). The image shows a sharp interface between the LSMO and BFO, suggesting that cationic mixing at the interface is minimal. The map in Fig. 1(b) is the 2D representation of the values of the pseudocubic lattice parameter *c* (normal to the interface) calculated from atomic column positions in (a); the increase from LSMO to BFO can be easily seen. The map shows a local increase in the pseudocubic *c* parameter in the first 3–4 layers of BFO adjacent to the interface. Note that this increase is localized near the interface and hence cannot be accounted for by the usual volume-conserving Poisson distortion due to epitaxial strain, which would act throughout the entire thickness of the film. The line plot in Fig. 1(c) shows that the lattice parameter in the first ~3–4 layers of BFO becomes as high as 4.21 Å before settling down at a value of ~4.06 Å after the first 4 layers, which is consistent with the value of 4.07 Å observed from x-ray diffraction data. There is no detectable change in the average of the lattice parameter parallel to the interface, consistent with a high-quality, pseudomorphically con-

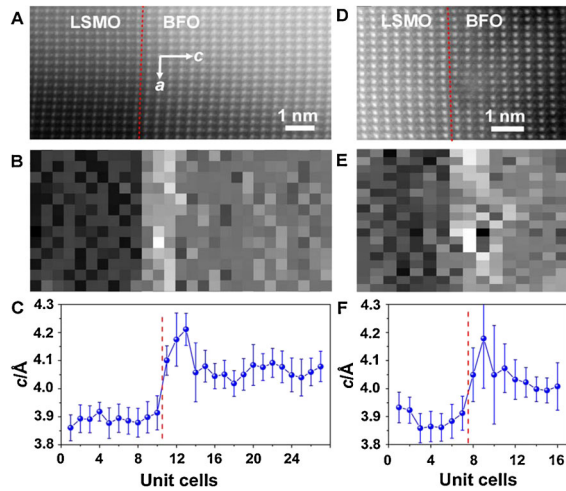


FIG. 1 (color online). Lattice parameters from HAADF STEM: (a) image of the STO/5 nm LSMO/50 nm BFO thin film, (b) corresponding 2D map of the c lattice parameter (normal to the interface), with lighter color corresponding to higher c values, (c) line profile obtained by averaging all rows of the map in (b) showing an increase in the first few layers of BFO. (d) Image of the STO/5 nm LSMO/3.2 nm BFO ultrathin film, (e) corresponding 2D map of the c lattice parameter, (f) line profile obtained by averaging all rows of the map in (e). Image in (d) was rescaled to correct for drift; error bars in (c) and (f) reflect variance between individual rows in the 2D maps. Note that graphs (c) and (f) are presented on the same absolute scale.

strained film. Identical behavior, up to and including the numerical value of the increased c parameter, is observed in ultrathin STO/5 nm LSMO/3.2 nm BFO film [Figs. 1(d)–1(f)]. Note that Bea *et al.* [14] observed a giant axial c/a distortion induced in a BFO film by compressive epitaxial strain throughout the film, whereas in our case the large distortion is limited to the interface layers.

To complement the analysis of the strains, we explore the octahedral tilts in the vicinity of the interface. We determine the tilt angles from the absolute positions of the Bi columns in two dimensions obtained from the HAADF STEM image in Fig. 1(d), and the oxygen columns obtained from a simultaneously-acquired bright field (BF) STEM image, given in Fig. 2(a). The two-dimensional tilt angle map in Fig. 2(b) shows a characteristic checkerboard pattern, consistent with the (001) projection of rhombohedral BFO [Fig. 2(c)]. Extensive investigation of the potential errors due to tilt and defocus indicated that such systematic errors were negligible compared to the experimental statistical errors [8]. The behavior of the tilt angles on even and odd sites in the lattice as a function of separation from the interface is shown in Fig. 2(d). Notice that the absolute values of tilt angles increase gradually in the BFO phase over ~ 4 –5 atomic layers, the same region that shows the expanded c -lattice parameter in Fig. 1(f). The saturated value of the tilt angle ($\sim 7^\circ$) far from the interface is approaching the value for bulk BFO (the projected $\theta_{\text{BFO}} \sim 10^\circ$ in this viewing direction).

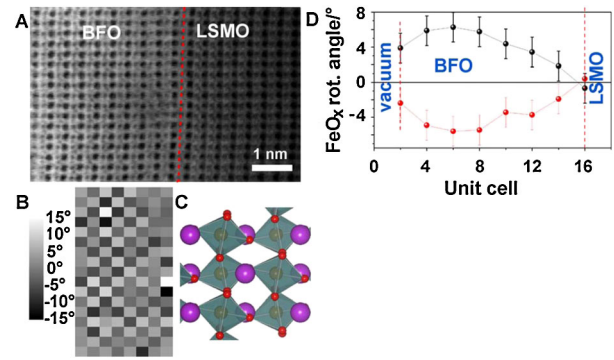


FIG. 2 (color online). Oxygen octahedral rotation angles from BF STEM: (a) image of the 3.2 nm BFO/5 nm LSMO/STO ultrathin film, acquired simultaneously with the HAADF image in Fig. 1(d), (b) corresponding 2D map of in-plane octahedral rotation angles in BFO showing checkerboard order (color scale on left); (c) BFO structure in rhombohedral (001) orientation showing the tilt pattern, (d) line profiles obtained from the map in (b) with two checkerboard “sublattices” added up separately: odd (top) and even (bottom); two bad points in the map corresponding to a hole in the sample are taken out of the averaging. The image in (a) was rescaled to correct for drift; the map in (b) was corrected for local Bi-Bi angle variations; error bars in (d) are equal to the standard deviation of local Bi-Bi angles.

Insight into chemical composition and local dielectric properties of the interface comes from an EELS image of the heterostructure [Fig. 3]. The energy range of -10 –350 eV includes the zero-loss peak (around 0 eV)

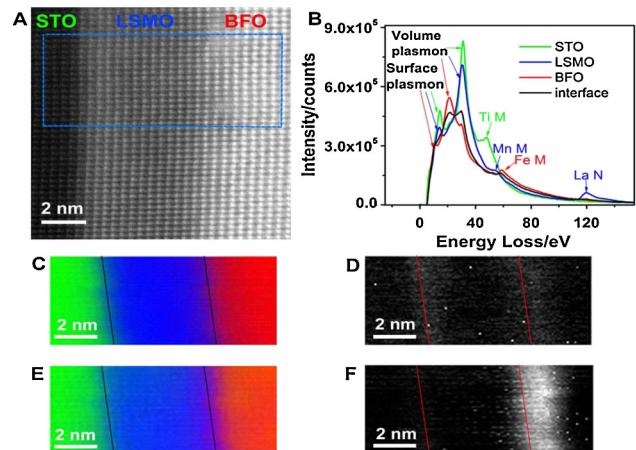


FIG. 3 (color online). Low-loss EELS imaging of the SrTiO₃/(La, Sr)MnO₃/BiFeO₃ interface. (a) imaging area; (b) representative spectra (after Fourier-log deconvolution) of the three components showing distinctive signatures and features; (c)–(f) results of the multiple least square fit of the image using BFO, LSMO, and STO spectra from (b) in two energy ranges: core loss (35 to 125 eV): (c) fit coefficient map, (d) χ^2 map; and plasmonic (5 to 35 eV): (e) fit coefficient map, and (f) χ^2 map. A region of BFO approximately 2 nm wide shows an anomaly in map (f). Thin lines denote interface positions taken from a simultaneously acquired dark field image. The interfaces appear tilted due to specimen drift during spectrum image acquisition (over 5 min).

and core-loss edges (Ti M, Mn M, Fe M, La N) at ≥ 35 eV. In the intermediate energy range (~ 5 to 30 eV), the electron energy losses are dominated by plasmon generation, and hence contain information on the dielectric function, dielectric properties, and electron density [7,15]. The suitability of these energy ranges (“low-loss EELS”) to generating spatially resolved data is sometimes questioned; however, recent work by Nelayah *et al.* [16] demonstrates clear nm-level localization for peaks in the 1–5 eV energy range; localization improves with increasing energy loss [7].

Figure 3(b) shows typical spectra (after Fourier-log deconvolution) from the three regions of the image and identifies different spectral features. From Fourier-log analysis, the sample thickness was quite uniform within the image (~ 50 nm), providing optimal conditions for low-loss imaging at which volume plasmonic excitations dominate. Clear differences are seen in both the plasmon energy and shape, and in the core-loss region, between the STO, LSMO, and BFO regions. To explore spatial variability of electronic structure and chemical composition at the interface, we used multiple least squares fitting. In this method, the local spectra are represented as a linear combination of the bulk phase spectra,

$$S(E, \mathbf{r}) = \alpha(\mathbf{r})S_{\text{LSMO}}(E) + \beta(\mathbf{r})S_{\text{BFO}}(E) + \gamma(\mathbf{r})S_{\text{STO}}(E) + S_D(E, \mathbf{r}). \quad (1)$$

Here, $S_{\text{LSMO}}(E)$, $S_{\text{BFO}}(E)$, and $S_{\text{STO}}(E)$ are the EELS spectra corresponding to the bulk phases of corresponding oxides, and $\alpha(\mathbf{r})$, $\beta(\mathbf{r})$, and $\gamma(\mathbf{r})$ are maps of corresponding linear coefficients. The error term $S_D(E, \mathbf{r})$ describes how well the local spectrum follows the linear superposition model; deviation can also be represented as χ^2 .

Fourier-log deconvolved spectra of the BFO, LSMO, and STO averaged over regions away from the interface were used as a basis; these spectra are shown in Fig. 3(b) (see figure legend). The decomposition by Eq. (1) was performed separately in two different energy ranges corresponding to different interactions: core-loss range (35 to 125 eV) and plasmonic range (5 to 35 eV). Figures 3(c)–3(e) show the fitting results for the core-loss range. The fit coefficient map [Fig. 3(c)] shows the clear contrast associated with individual phases, i.e., provides chemical identification of the components. The spatial resolution of this map as determined by the 25%–75% criterion [17] is ~ 0.8 nm. It is in good agreement with the simultaneously acquired ADF image, and the map of the χ^2 [Fig. 3(e)] shows no anomalies. Note that due to close proximity of the Ti, Mn, and Fe M edges and plasmon peaks, the chemical identification problem is not accessible by standard background subtraction. Studies using atomic column resolved EELS (not shown) confirmed that chemically both interfaces are sharp within experimental precision. At the same time, in the plasmonic energy range the χ^2 map [Fig. 3(f)] shows an anomalous band, indicating that in this energy range the EELS spectra of the interface region

cannot be interpreted as a linear superposition of constituents, suggesting the presence of a layer with anomalous dielectric properties. The band is located over the first ~ 2 nm (5 unit cells) of the BFO, and closely coincides with the width of the strained layer. This anomaly can be observed in the EELS images of both thick (50 nm) and thin (3.2 nm) films, and in films with different polarization orientations. In comparison, the STO-LSMO interface is identified as abrupt (within the resolution) in both energy ranges.

The comparison of EELS (anomalous layer) and structural (tilt angle, lattice expansion) data suggests that the origins of the observed behavior lie in the coupling of the antiferrodistortive order parameter (i.e., octahedral tilts) across the interface. Indeed, the propagation of the zone boundary modes [18] and closure polarization patterns [19] across the interface has been demonstrated as an effective mechanism for stabilization of polarization in the ferroelectric-oxide heterostructures. Similarly, the coupling of the antiferrodistortive order parameter plays a crucial role in the STO-LaTiO₃ system [20,21] and the STO-LaAlO₃ system [22]. The continuity of the octahedral sublattice requires tilt angles to be continuous across the interface. Since the octahedral tilts in LSMO are much smaller (due to the proximity of STO substrate) and are close to zero at the interface (see Fig. S3 in [8]), the BFO tilt angle is suppressed at the interface. Note that relaxation of the tilt angle can proceed only through deformation of the octahedra, i.e., direct change in the electronic structure of the central cation. Hence, the interfacial electronic property is expected to be greatly influenced by these structural changes. The increase of the Fe-O-Fe angle (towards 180°) and forced higher symmetry is expected to increase the bandwidth of occupied and unoccupied bands, reducing the band gap in the BFO.

Density functional theory (DFT) calculations support this conjecture. We conducted both local spin-density approximation (LSDA) and LSDA + U calculations of the bulk BFO band structure, consistent with those performed previously [23]. In both cases, forcing BFO into tilt-free cubic symmetry significantly reduces the band gap. In the case of LSDA, the band gap changes from 0.40 eV to 0, and the ground state becomes ferromagnetic, rather than G -type antiferromagnetic [Fig. 4(a)]. For LSDA + U , we have chosen $U_{\text{eff}} = 3.0$ eV, which gives a direct band gap of 2.5 eV at the Γ point, compared to the experimental direct band gap of 2.7 eV [24]. The calculated indirect gap is reduced from 1.7 to 0.74 eV on suppressing the octahedral tilts; the ground state remains G -type antiferromagnetic and insulating [Fig. 4(b)]. In both the LSDA and LSDA + U cases we find that the decrease in the band gap comes mainly from an enhancement of the bandwidth, especially of the unoccupied Fe minority-spin d states. This is consistent with an increase in the Fe-O-Fe angle to 180° with suppressed octahedral tilting, which increases interatomic hopping and therefore the bandwidth.

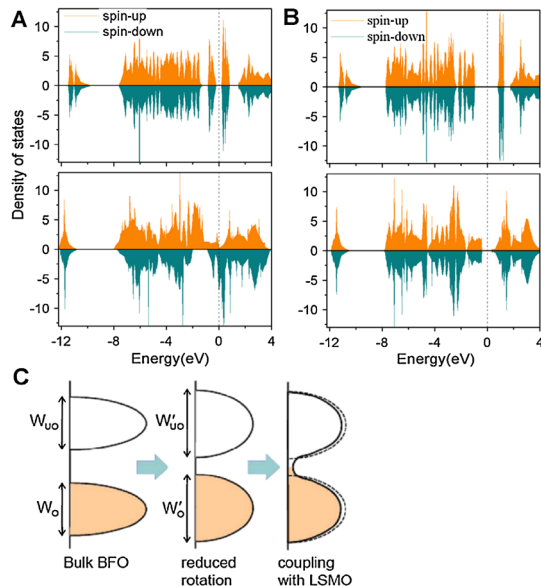


FIG. 4 (color online). Interfacial lattice distortion in BiFeO_3 and its effect on the density of states. (a) DOS by LSDA method, in fully relaxed BiFeO_3 (top) where oxygen octahedron rotations are present and (bottom) in cubic BiFeO_3 where oxygen octahedron rotations are absent; band gap is reduced from 0.44 to 0 eV. (b) DOS by LSDA + U method, $U - J = 3.0$ eV (top) in fully relaxed BiFeO_3 where oxygen octahedron rotations are present and (bottom) in cubic BiFeO_3 where oxygen octahedron rotations are absent; band gap is reduced from 1.7 to 0.74 eV. The dashed lines indicate the position of the Fermi energy. (c) Additional coupling with LSMO can generate finite density of states within the gap.

Notably, the distortion of the BFO itself is not the only possible source of changes to the electronic structure at this interface. For instance, evanescent wave function tails from the LSMO penetrate into the BFO introducing a finite density of metal induced gap states (MIGS) [25]. The finite density of states (DOS) further enhances the conductive behavior [Fig. 4(c)]. It is, however, not possible to attribute the altered dielectric behavior at the interface entirely to MIGS, as the spatial extent of these states is expected to be much smaller than 2 nm (see [8]).

These studies demonstrate the new paradigm of an interface phase transition mediated by the antiferrodistortive coupling across the interface, complementing the established polarization- and charge driven behavior. This also implies that novel ferromagnetic properties can arise in the vicinity of the interface as the result of the deformation of oxygen octahedral surrounding cation and changes in M-O-M angles, as confirmed by a recent study using x-ray magnetic circular dichroism measurements [26] (also see [8]). These results illustrate that controlling the octahedral tilting behavior can provide a new, and virtually unexplored, dimension to the behavior of the ferroelectric and multiferroic films. Selectively tuning (either suppressing or enhancing) the tilts using the appropriate substrates can thus be used to establish new phases with novel properties, extending the concept of the strain- and polarization

controlled interfaces to a broad new class of tilt-controlled phenomena.

The research is sponsored by the Division of Materials Sciences and Engineering, Office of Basic Energy Sciences, U.S. Department of Energy (A. Y. B., S. V. K., and S. O.), and by appointment (H. J. C.) to the ORNL Postdoctoral Research Program administered jointly by ORNL and ORISE. The work at Berkeley is partially supported by the Semiconductor Research Corporation as well as by the U.S. DOE under Contract No. DE-AC02-05CH1123. The work at Nebraska is supported by the NSF-funded MRSEC (Grant No. DMR-0820521), the Nanoelectronics Research Initiative of the Semiconductor Research Corporation and the Nebraska Research Initiative. Computations were performed utilizing the Research Computing Facility at UNL and the Center for Nanophase Materials Sciences at ORNL.

*albinab@ornl.gov

- [1] A. Ohtomo and H. Y. Hwang, *Nature (London)* **427**, 423 (2004).
- [2] N. Reyren *et al.*, *Science* **317**, 1196 (2007).
- [3] A. Brinkman *et al.*, *Nature Mater.* **6**, 493 (2007).
- [4] E. Bousquet *et al.*, *Nature (London)* **452**, 732 (2008).
- [5] C. L. Jia *et al.*, *Nature Mater.* **6**, 64 (2007).
- [6] C. L. Jia *et al.*, *Nature Mater.* **7**, 57 (2008).
- [7] R. F. Egerton, *Electron Energy Loss Spectroscopy in the Electron Microscope* (Springer, New York, 1996).
- [8] See supplementary material at <http://link.aps.org/supplemental/10.1103/PhysRevLett.105.087204> for additional details of synthesis, data analysis, and theory.
- [9] S. Lisenkov, D. Rahmedov, and L. Bellaiche, *Phys. Rev. Lett.* **103**, 047204 (2009).
- [10] I. Ponomareva and L. Bellaiche, *Phys. Rev. Lett.* **101**, 197602 (2008).
- [11] R. Palai *et al.*, *Phys. Rev. B* **77**, 014110 (2008).
- [12] G. Catalan and J. F. Scott, *Adv. Mater.* **21**, 2463 (2009).
- [13] C. L. Jia *et al.*, *Phys. Rev. B* **79**, 081405 (2009).
- [14] H. Bea *et al.*, *Phys. Rev. Lett.* **102**, 217603 (2009).
- [15] F. J. Garcia de Abajo, *Rev. Mod. Phys.* **82**, 209 (2010).
- [16] J. Nelayah *et al.*, *Nature Phys.* **3**, 348 (2007).
- [17] L. Reimer and H. Kohl, *Transmission Electron Microscopy: Physics of Image Formation* (Springer, New York, 2008).
- [18] G. Gerra, A. K. Tagantsev, N. Setter, and K. Parlinski, *Phys. Rev. Lett.* **96**, 107603 (2006).
- [19] P. Aguado-Puente and J. Junquera, *Phys. Rev. Lett.* **100**, 177601 (2008).
- [20] S. Okamoto, A. J. Millis, and N. A. Spaldin, *Phys. Rev. Lett.* **97**, 056802 (2006).
- [21] D. R. Hamann, D. A. Muller, and H. Y. Hwang, *Phys. Rev. B* **73**, 195403 (2006).
- [22] P. R. Willmott *et al.*, *Phys. Rev. Lett.* **99**, 155502 (2007).
- [23] J. B. Neaton *et al.*, *Phys. Rev. B* **71**, 014113 (2005).
- [24] J. F. Ihlefeld *et al.*, *Appl. Phys. Lett.* **92**, 142908 (2008).
- [25] V. Heine, *Phys. Rev.* **138**, A1689 (1965).
- [26] P. Yu *et al.*, *Phys. Rev. Lett.* **105**, 027201 (2010).